The Astrophysical Journal Letters, 926:L16 (9pp), 2022 February 20 https://doi.org/10.3847/2041-8213/ac51da

Turbulence in the Sub-Alfvénic Solar Wind

G. P. Zank[1], L.-L. Zhao[1], L. Adhikari[1], D. Telloni[2], J. C. Kasper[3], M. Stevens[4], A. Rahmati[5], and S. D. Bale[6]
[1] Center for Space Plasma and Aeronomic Research (CSPAR) and Department of Space Science, University of Alabama in Huntsville, Huntsville, AL 35805, USA
garyp.zank@gmail.com
[2] INAF–Astrophysical Observatory of Torino, Via Osservatorio 20, I-10025 Pino Torinese, Italy
[3] BWX Technologies, Inc., Washington, DC 20002, and Department of Climate and Space Sciences and Engineering, University of Michigan, Ann Arbor, MI 48109, USA
[4] Smithsonian Astrophysical Observatory, Cambridge, MA 02138, USA
[5] Space Sciences Laboratory, University of California, Berkeley, CA 94720-7300, USA
[6] Physics Department, University of California, Berkeley, CA 94720-7300, USA
Received 2021 December 8; revised 2022 February 2; accepted 2022 February 3; published 2022 February 18

Abstract

The Parker Solar Probe (PSP) entered a region of sub-Alfvénic solar wind during encounter 8, and we present the first detailed analysis of low-frequency turbulence properties in this novel region. The magnetic field and flow velocity vectors were highly aligned during this interval. By constructing spectrograms of the normalized magnetic helicity, cross-helicity, and residual energy, we find that PSP observed primarily Alfvénic fluctuations, a consequence of the highly field-aligned flow that renders quasi-2D fluctuations unobservable to PSP. We extend Taylor's hypothesis to sub- and super-Alfvénic flows. Spectra for the fluctuating forward and backward Elsässer variables ($z^{\pm}$, respectively) are presented, showing that z^{+} modes dominate z^{-} by an order of magnitude or more, and the z^{+} spectrum is a power law in frequency (parallel wavenumber) $f^{-3/2}$ ($k_{\parallel}^{-3/2}$) compared to the convex z^{-} spectrum with $f^{-3/2}$ ($k_{\parallel}^{-3/2}$) at low frequencies, flattening around a transition frequency (at which the nonlinear and Alfvén timescales are balanced) to $f^{-1.25}$ at higher frequencies. The observed spectra are well fitted using a spectral theory for nearly incompressible magnetohydrodynamics assuming a wavenumber anisotropy $k_{\perp} \sim k_{\parallel}^{3/4}$, that the z^{+} fluctuations experience primarily nonlinear interactions, and that the minority z^{-} fluctuations experience both nonlinear and Alfvénic interactions with z^{+} fluctuations. The density spectrum is a power law that resembles neither the $z^{\pm}$ spectra nor the compressible magnetic field spectrum, suggesting that these are advected entropic rather than magnetosonic modes and not due to the parametric decay instability. Spectra in the neighboring modestly super-Alfvénic intervals are similar.

Unified Astronomy Thesaurus concepts: Interplanetary turbulence (830); Solar wind (1534); Solar physics (1476); Solar coronal waves (1995); Solar corona (1483)

1. Introduction

For about 5 hr between 09:30 and 14:40 UT on 2021 April 28 at around 0.1 au, the NASA Parker Solar Probe (PSP) entered a sub-Alfvénic region of the solar wind (Kasper et al. 2021). Two further shorter sub-Alfvénic intervals were subsequently sampled during encounter 8. Kasper et al. (2021) ascribed the first sub-Alfvénic region to a steady flow in a region of rapidly expanding magnetic field above a pseudostreamer. The discovery of this hitherto in situ unobserved region of the solar wind represents a major accomplishment of the PSP mission, particularly for the insight it will provide into our understanding of how the solar corona is heated and the solar wind accelerated. The dissipation of low-frequency turbulence is regarded as a promising mechanism for heating the solar corona. The current explicitly turbulence models come in essentially two flavors; one of them is dominated by outwardly propagating Alfvén waves, a sufficient number of which are reflected by the large-scale coronal plasma gradient to produce a counterpropagating population of Alfvén waves that interact nonlinearly to produce zero-frequency modes that cascade energy nonlinearly to the dissipation scale to heat the corona (Matthaeus et al. 1999; Verdini et al. 2009; Cranmer & van Ballegooijen 2012; Shoda et al. 2018; Chandran & Perez 2019). The second approach recognizes that magnetohydrodynamics (MHD) in the plasma beta $\beta_p \equiv P/(B^2/2/\mu_0) \ll 1$ or $O(1)$ regimes (where P is the plasma pressure, $B = |\boldsymbol{B}|$, $\boldsymbol{B}$ is the magnetic field, and μ_0 is the magnetic permeability) is quasi-2D at leading order (Zank & Matthaeus 1992, 1993), with the result that turbulence in these regimes is dominated by quasi-2D turbulence with a minority slab turbulence component (Zank et al. 2017). Nearly incompressible MHD (NI MHD) is the foundation of the well-known 2D+slab superposition model for turbulence in the solar wind (Matthaeus et al. 1990; Bieber et al. 1994, 1996). The NI MHD description forms the basis of the coronal turbulence heating model advocated by Zank et al. (2018) for which a dominant population of turbulent MHD structures (flux ropes/magnetic islands, vortices, plasmoids) is generated in the magnetic carpet of the photosphere and advected through and dissipated in the low corona. Accompanying the majority quasi-2D turbulence is a minority population of Alfvénic or slab turbulence, most likely predominantly outward-propagating. A comparative analysis of the two turbulence models using PSP observations is presented in Zank et al. (2021). Here we examine the properties of low-frequency MHD turbulence in the first sub-Alfvénic interval observed by PSP and show that these observations admit a natural interpretation in terms of the NI MHD spectral theory (Zank et al. 2020).

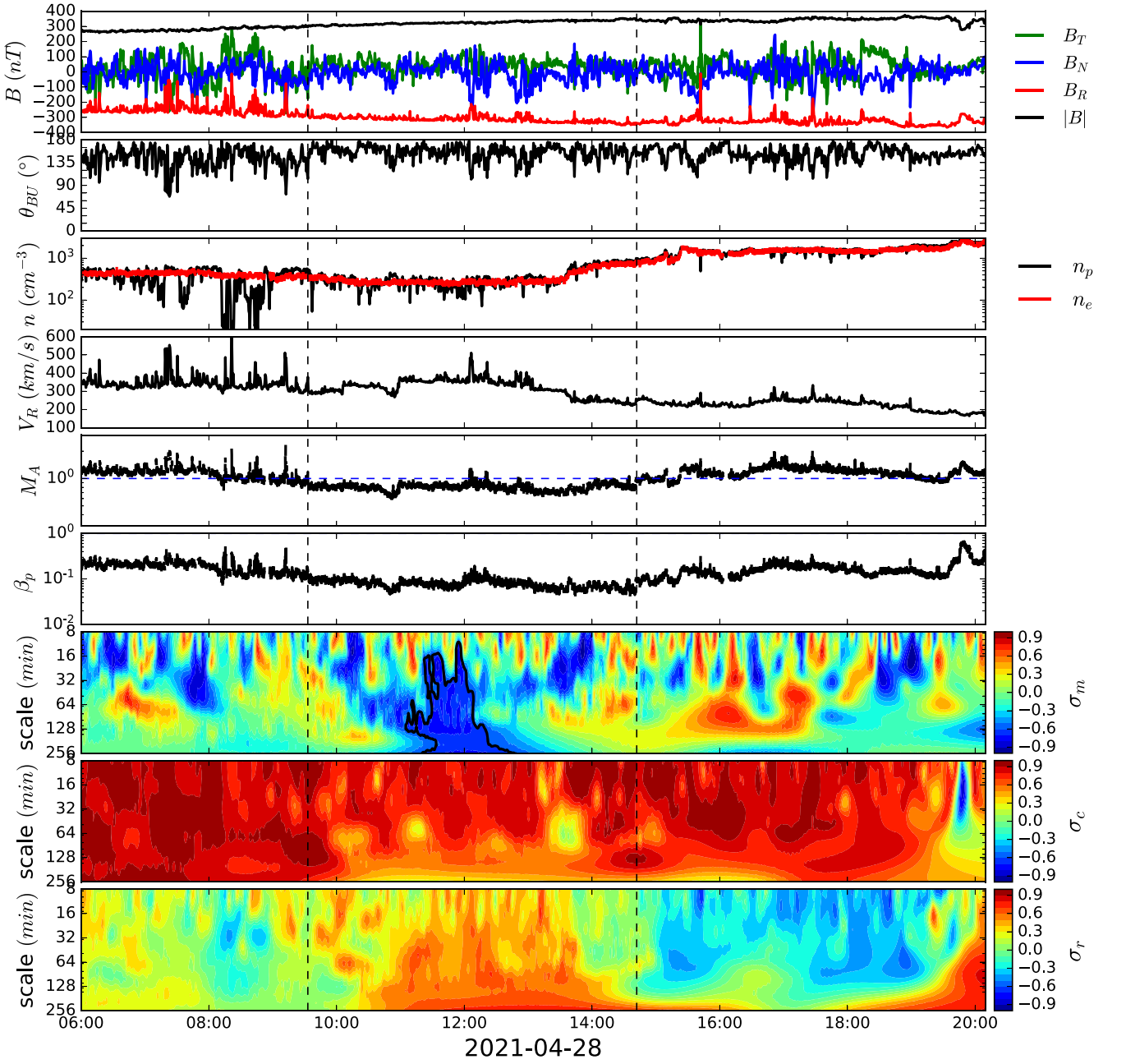

Figure 1. Overview of the first sub-Alfvénic interval, located between the dashed vertical lines, and the adjacent super-Alfvénic intervals observed by PSP during encounter 8, showing (top to bottom) the radial B_R, transverse B_T, and normal B_N magnetic fields and intensity $|\boldsymbol{B}|$; the angle θ_{BU} between the relative flow velocity $\boldsymbol{U}_0$ (i.e., the relative velocity between the solar wind flow and the spacecraft velocity vectors) and magnetic field vectors; the proton n_p (black) and electron number density n_e (red); the radial component of the plasma speed V_R measured in the inertial RTN frame; the Alfvénic Mach number of the radial flow $M_A = V_R/V_A$; and the plasma beta β_p. The bottom three colored panels, in descending order, show frequency spectrograms of the normalized magnetic helicity σ_m, normalized cross-helicity σ_c, and normalized residual energy σ_r.

Figure 1 is an overview of the first and longest of three sub-Alfvénic intervals identified by Kasper et al. (2021). The data we used include magnetic field measurements from PSP/FIELDS (Bale et al. 2016), ion moment data from the PSP/SWEAP instrument, and electron density derived from quasi-thermal noise spectroscopy (Kasper et al. 2016, 2021). The radial magnetic field is extremely steady with relatively small amplitude fluctuations. The radial velocity is also rather steady, and the alignment between the flow and magnetic field vectors is very high. Below, we introduce the quantity $\Psi \equiv \langle \theta_{B_0 U_0} \rangle$, where $\boldsymbol{B}_0$ and $\boldsymbol{U}_0$ are the magnetic and plasma velocity mean fields during the intervals of interest. The velocity $\boldsymbol{U}_0$ is the relative velocity that includes the spacecraft speed, i.e., the spacecraft frame velocity. As we discuss in Section 2, this is important for the generalized form of Taylor's hypothesis that we use. The flow appears to be mostly sub-Alfvénic, although relatively marginally, across much of the interval, since the Alfvénic Mach number $M_A = V_R/V_A \lesssim 1$. That the flow is so highly aligned renders quasi-2D fluctuations essentially invisible to PSP, as we show explicitly below, and only fluctuations propagating along or antiparallel to the inwardly directed (toward the Sun) magnetic field are observable. The plasma beta β_p is well below 1, being close to 10^{-1} for most of the interval. In the NI MHD context, this would imply that the

predicted majority quasi-2D component was not observed because of the close alignment of the flow with the magnetic field; instead, the observed fluctuations correspond to a minority slab component.

We have developed a method (Zhao et al. 2019, 2020b) to automatically identify magnetic flux ropes and Alfvénic fluctuations based on the observed rotation of the magnetic field (Burlaga et al. 1981; Moldwin et al. 1995) and the normalized reduced magnetic helicity (Matthaeus et al. 1982), which is usually high in regions of magnetic flux ropes (Telloni et al. 2012, 2013). To distinguish between Alfvénic structures and flux ropes, we evaluate the normalized cross-helicity σ_c ($\equiv(\langle z^{+2}\rangle - \langle z^{-2}\rangle)/(\langle z^{+2}\rangle + \langle z^{-2}\rangle)$), where $\boldsymbol{z}^{\pm} = \boldsymbol{u} \pm \boldsymbol{b}/\sqrt{\mu_0\rho}$ are the Elsässer variables for the fluctuating velocity $\boldsymbol{u}$ and magnetic $\boldsymbol{b}$ fields and ρ is the mean plasma density, and the normalized residual energy σ_r ($\equiv \langle \boldsymbol{z}^{+}\cdot\boldsymbol{z}^{-}\rangle/(\langle z^{+2}\rangle + \langle z^{-2}\rangle) = (\langle u^2\rangle - \langle b^2\rangle/(\mu_0\rho))/(\langle u^2\rangle + \langle b^2\rangle/(\mu_0\rho))$). In most cases, the cross-helicity of a magnetic flux rope is low (because of their closed-loop field structure, implying both sunward and antisunward Alfvénic fluctuations inside), and the residual energy is negative (indicating the dominance of magnetic fluctuation energy), whereas Alfvénic structures typically exhibit high cross-helicity and small residual energy values. Frequency spectrograms of the normalized magnetic helicity σ_m, normalized cross-helicity σ_c, and normalized residual energy σ_r are illustrated in the bottom three panels of Figure 1. Several points are immediately apparent. There are numerous small and mid-scale magnetic positive and negative rotations, including a particularly large structure bounded by black contour lines with $\langle\sigma_m\rangle \simeq -0.7$. Within this high magnetic helicity structure, the average σ_c is around 0.55, and the average σ_r is about 0.5. The scale size of this structure is around 80 minutes. The plasma outside this large structure has a cross-helicity close to 1, indicating almost exclusively outward-propagating, antiparallel to the mean magnetic field Elsässer fluctuations $\boldsymbol{z}^{+}$. The residual energy spectrogram shows large regions with $\sigma_r \simeq 0$, i.e., Alfvénic fluctuations, although the border region near 16:00 hr, 2021 April 28, appears to be comprised of largely magnetic structures with negative σ_r. The left-handed helical structure ($\sigma_m < 0$) at about 12:00 has a positive σ_r (~0.5), indicating the relative dominance of kinetic fluctuating energy. It suggests that PSP may have observed a vortical structure with a relatively weak wound-up magnetic field.

The combination of $\sigma_c \sim 0.9$ and $\sigma_r \sim 0.0$ for much of the sub-Alfvénic interval suggests that, not surprisingly, PSP is observing primarily Alfvénic fluctuations. This is typically described as "Alfvénic turbulence" despite the inability of PSP to easily discern non-Alfvénic structures in a highly magnetic field-aligned flow. The very high value of σ_c raises considerable problems for slab turbulence, which relies on counter-propagating Alfvén waves to generate the nonlinear interactions that allow for the cascading of energy to ever smaller scales (Dobrowolny et al. 1980a, 1980b; Shebalin et al. 1983). Such highly field-aligned flows with high σ_c and populated by unidirectionally propagating Alfvén waves have been observed near 1 au (Wang et al. 2015; Telloni et al. 2019) by the Wind spacecraft and closer to the Sun by PSP (Zhao et al. 2020a, 2021a). The 1D reduced spectra in both cases exhibited a $k_{\parallel}^{-5/3}$ form in the inertial range (where $k_{\parallel}$ is the wavenumber parallel to the mean magnetic field), raising questions about the validity of the critical balance theory (Goldreich & Sridhar 1995; Telloni et al. 2019). The spectral theory of NI MHD in the $\beta_p \ll 1$ and ~1 regimes (Zank et al. 2020) shows that the interaction of a dominant quasi-2D component with unidirectional Alfvén waves can yield a $k_{\parallel}^{-5/3}$ spectrum. The sub-Alfvénic interval of Figure 1 exhibits a number of features quite similar to those observed in the highly field-aligned flows discussed by Telloni et al. (2019) and Zhao et al. (2020a, 2021a).

In this Letter, we analyze the turbulent properties of the sub-Alfvénic interval shown in Figure 1 in more detail than in Kasper et al. (2021) and interpret the observations based on the NI MHD spectral theory appropriate to the anisotropic superposition of quasi-2D+slab turbulence (Zank et al. 2020). This does, however, require the correct application of Taylor's hypothesis for the sub-Alfvénic and modestly super-Alfvénic flows discussed here. Such an extension is straightforwardly developed in the context of the NI MHD superposition model, but it does require that the $\boldsymbol{z}^{\pm}$ Elsässer modes be treated separately for the minority forward- and backward-propagating slab modes. This is done in the following section, after which we apply the results to the $\boldsymbol{z}^{\pm}$ spectra observed by PSP.

2. Relating Wavenumber and Frequency Spectra

Taylor's hypothesis assumes that a simple Galilean transformation, $\omega = \boldsymbol{U}_0\cdot\boldsymbol{k}$, can relate the wavenumber $\boldsymbol{k}$ in the inertial frame to the observed frequency (ω or $2\pi f$). Here we assume implicitly that $\boldsymbol{U}_0$ is the relative velocity between the background solar wind flow velocity and the spacecraft velocity. This is reasonable in the fully developed supersonic solar wind, where one can assume that characteristic wave speeds are $\ll\boldsymbol{U}_0$, particularly the Alfvén velocity that satisfies $|\boldsymbol{V}_A\cdot\boldsymbol{k}| \ll |\boldsymbol{U}_0\cdot\boldsymbol{k}|$, but Taylor's hypothesis is unlikely to be appropriate to sub-Alfvénic or modestly super-Alfvénic regions of the solar wind. Suppose that $\boldsymbol{x} = (V_p + \boldsymbol{U}_0)t = \boldsymbol{V}t$, $\boldsymbol{x}' = \boldsymbol{x} + \boldsymbol{\ell}, t' = t + \tau$, where $\boldsymbol{\ell}$ and τ are spatial and temporal separations from $\boldsymbol{x}$ and t, and $\boldsymbol{V}_p$ denotes a phase velocity. On making the usual assumptions of homogeneity and stationarity, it is straightforward to show that the power spectral density (PSD) is (Bieber et al. 1996; Saur & Bieber 1999; Zank et al. 2020)

$$P_{ij}(f) = \int e^{i2\pi f\tau}\int P_{ij}(\boldsymbol{k})e^{-i\boldsymbol{k}\cdot\boldsymbol{V}\tau}d\boldsymbol{k}d\tau. \quad (1)$$

For 2D modes that experience only advection, $\omega = 0$, whereas for slab/Alfvénic turbulence, $\omega = \pm V_A k_{\parallel} = \pm V_A k_z$. For 2D turbulence, since $V_p = 0$, we have simply

$$P_{ij}^{\infty}(f) = \int e^{i2\pi f\tau}\int P_{ij}^{\infty}(\boldsymbol{k})e^{-i\boldsymbol{k}\cdot\boldsymbol{U}_0\tau}d\boldsymbol{k}d\tau. \quad (2)$$

For slab turbulence, we need to decompose the fluctuations into forward- (+) and backward- (−) propagating modes (some care needs to be exercised in practice relative to the mean magnetic field orientation). On extending Zank et al. (2020), the slab PSD is given by

$$P_{ij}^{*\pm}(f) = \int e^{i2\pi f\tau}\int P_{ij}^{*\pm}(\boldsymbol{k})e^{-i(\mp V_A k_z + \boldsymbol{U}_0\cdot\boldsymbol{k})\tau}d\boldsymbol{k}d\tau, \quad (3)$$

with $\mp V_A$ appearing in the exponential because, formally, the $\boldsymbol{z}^{*+}$ transport equation contains the advection term $(\boldsymbol{U} - \boldsymbol{V}_A)\cdot\nabla$, and the $\boldsymbol{z}^{*-}$ transport equation has $(\boldsymbol{U} + \boldsymbol{V}_A)\cdot\nabla$ (Zank et al. 2017). Other approaches to Taylor's hypothesis

that are not based on an assumed 2D+slab decomposition of the turbulence have been considered (e.g., Klein et al. 2015; Bourouaine & Perez 2020). We comment that although the generalized form of Taylor's hypothesis used here (based on a 2D+slab decomposition) accounts for the z^+ component (propagating at a phase speed of $\boldsymbol{U}-\boldsymbol{V}_A$) and the z^- component associated with a phase speed ($\boldsymbol{U}+\boldsymbol{V}_A$), we do not account for the "anomalous" z^- component arising from reflection and "mixing" from large-scale flow gradients and z^+.

Following Bieber et al. (1996), we approximate $P_{ij}^{\infty,*\pm}(\boldsymbol{k})$ by general forms of the 2D (∞) and forward and backward slab ($^*\pm$) spectral tensors (Equations (4) and (5) in Zank et al. 2020; Matthaeus & Smith 1981). The spectral theory developed in Zank et al. (2020) is for the Elsässer variables, and we therefore focus on the Elsässer representation for $P_{ij}^{\infty,*\pm}(\boldsymbol{k})$ here. It is reasonable to assume isotropy for the 2D fluctuations. On performing the suitable integrals, the 2D results of Zank et al. (2020) are unchanged (assuming isotropy), whereas for super-Alfvénic flows satisfying $U_0\cos\Psi > |V_A|$ (where the local mean magnetic field defines the $\hat{\boldsymbol{z}}$-axis, the $\hat{\boldsymbol{x}}$-axis is defined by the planes of the mean magnetic field $\boldsymbol{B}_0$ and $\boldsymbol{U}_0$, $\hat{\boldsymbol{y}}$ is orthogonal to the $\hat{\boldsymbol{x}}$-$\hat{\boldsymbol{z}}$-plane, and Ψ the angle between $\boldsymbol{B}_0$ and $\boldsymbol{U}_0$),

$$\begin{aligned} P_{xx}^{*\pm}(f) &= P_{\parallel}^{*\pm}(f) \\ &= \frac{C^{*\pm}}{2}\frac{2\pi}{U_0\cos\Psi \mp V_A}G^{*\pm}(k_z) \\ &= P_{yy}^{*\pm}(f) \\ &= P_{\perp}^{*\pm}(f), \\ k_z &= \frac{2\pi f}{U_0\cos\Psi \mp V_A}, \end{aligned} \tag{4}$$

where $C^{*\pm}$ are the amplitudes of the forward- and backward-propagating slab fluctuations. Here $G^{*\pm}(k_z)$ is the spectral expression for slab turbulence in the NI MHD $\beta_p \ll 1$, ~ 1 regime, was derived in Zank et al. (2020), and is discussed below. For sub-Alfvénic flows, we find

$$\begin{aligned} P_{xx}^{*\pm}(f) &= P_{\parallel}^{*\pm}(f) \\ &= \frac{C^{*\pm}}{2}\frac{2\pi}{V_A \mp U_0\cos\Psi}G^{*\pm}(k_z) \\ &= P_{yy}^{*\pm}(f) = P_{\perp}^{*\pm}(f), \\ k_z &= \frac{2\pi f}{V_A \mp U_0\cos\Psi}. \end{aligned} \tag{5}$$

Of course, $P_{\rm total}^{*\pm}(f) = P_{\parallel}^{*\pm}(f) + P_{\perp}^{*\pm}(f)$.

The composite spectra for super- and sub-Alfvénic flows are therefore given by Equations (6) and (7) and Equations (8) and (9), respectively, below:

$$\begin{aligned} P_{\parallel}^{\rm total\pm}(f) &= P_{\parallel}^{\infty}(f) + P_{\parallel}^{*\pm}(f) \\ &= \frac{C^{\infty}}{q^{\infty}+1}\left(\frac{U_0\sin\Psi}{2\pi}\right)^{q^{\infty}-1} f^{-q^{\infty}} \\ &\quad + \frac{C^{*\pm}}{2}\frac{2\pi}{U_0\cos\Psi \mp V_A}G^{*\pm}(k_z), \end{aligned} \tag{6}$$

$$\begin{aligned} P_{\perp}^{\rm total\pm}(f) &= P_{\perp}^{\infty}(f) + P_{\perp}^{*\pm}(f) \\ &= \frac{q^{\infty}}{q^{\infty}+1}C^{\infty}\left(\frac{U_0\sin\Psi}{2\pi}\right)^{q^{\infty}-1} f^{-q^{\infty}} \\ &\quad + \frac{C^{*\pm}}{2}\frac{2\pi}{U_0\cos\Psi \mp V_A}G^{*\pm}(k_z), \end{aligned} \tag{7}$$

and $k_z = 2\pi f/(U_0\cos\Psi \mp V_A)$, where C^{∞} is the amplitude of the 2D turbulence, and q^{∞} is the spectral index of the 2D component; and

$$\begin{aligned} P_{\parallel}^{\rm total\pm}(f) &= \frac{C^{\infty}}{q^{\infty}+1}\left(\frac{U_0\sin\Psi}{2\pi}\right)^{q^{\infty}-1} f^{-q^{\infty}} \\ &\quad + \frac{C^{*\pm}}{2}\frac{2\pi}{V_A \mp U_0\cos\Psi}G^{*\pm}(k_z), \end{aligned} \tag{8}$$

$$\begin{aligned} P_{\perp}^{\rm total\pm}(f) &= \frac{q^{\infty}}{q^{\infty}+1}C^{\infty}\left(\frac{U_0\sin\Psi}{2\pi}\right)^{q^{\infty}-1} f^{-q^{\infty}} \\ &\quad + \frac{C^{*\pm}}{2}\frac{2\pi}{V_A \mp U_0\cos\Psi}G^{*\pm}(k_z), \end{aligned} \tag{9}$$

and $k_z = 2\pi f/(V_A \mp U_0\cos\Psi)$. The spectral theory for $\beta_p \ll 1$, ~ 1 NI MHD predicts that the dominant 2D spectrum is a $-5/3$ power law in $k_\perp$, i.e., $G^{\infty}(k_\perp) \equiv E^{\infty}(k_\perp)k_\perp = C^{\infty}k_\perp^{-5/3}$ (Zank et al. 2017, 2020), where $E^{\infty}(k_\perp)$ is the 1D Elsässer energy spectrum. However, because the flow is so highly magnetically aligned ($\Psi \simeq 3^\circ$ in the sub- and super-Alfvénic regions of interest), $P_{\parallel}^{\infty}(f)$ and $P_{\perp}^{\infty}(f)$ are effectively zero. Thus, as described above, the quasi-perpendicular fluctuations are, unfortunately, essentially invisible to PSP measurements.

3. Observed Spectra and Theory

In Figure 2, we plot the PSDs of the forward and backward Elsässer variables $z^{\pm}$ for the sub-Alfvénic region (9:33–14:42 UT) and a neighboring super-Alfvénic region (15:00–20:10 UT). This super-Alfvénic region was used because the discrepancy between the ion partial moment density measured by SPAN and the electron density estimated from FIELDS is large in the preceding super-Alfvénic region (see Figure 1) due to part of the particle velocity distribution measured by SWEAP being blocked. The PSD is evaluated over a 5 hr interval for each region. We use the standard Fourier method to calculate the trace spectra of $z^{\pm}$ based on the Fourier-transformed autocorrelation function of the three components. The vertical dashed–dotted line in each panel denotes the frequency corresponding to the correlation scale that separates the energy-containing range and inertial range. An f^{-1} spectrum for the energy-containing range is displayed as a reference. The cyan and green curves in each panel are the theoretical predicted spectra for $z^{\pm}$ in both sub- and super-Alfvén regions. The dominant component in both regions is evidently the outward-propagating z^+ component, with the PSD being at least an order of magnitude larger than that of the inward z^- component. The flattening of the z^- PSD at frequencies $\geqslant 10^{-2}$ Hz has no physical significance and is due to the noise floor in the plasma measurements. Careful examination of the z^- PSD shows that the low-frequency part of the spectrum is steeper than the high-frequency part, whereas the z^+ PSD, other than a bump at the inner scale (Kasper et al. 2021), is a single power law in frequency with $\sim f^{-1.5}$. The

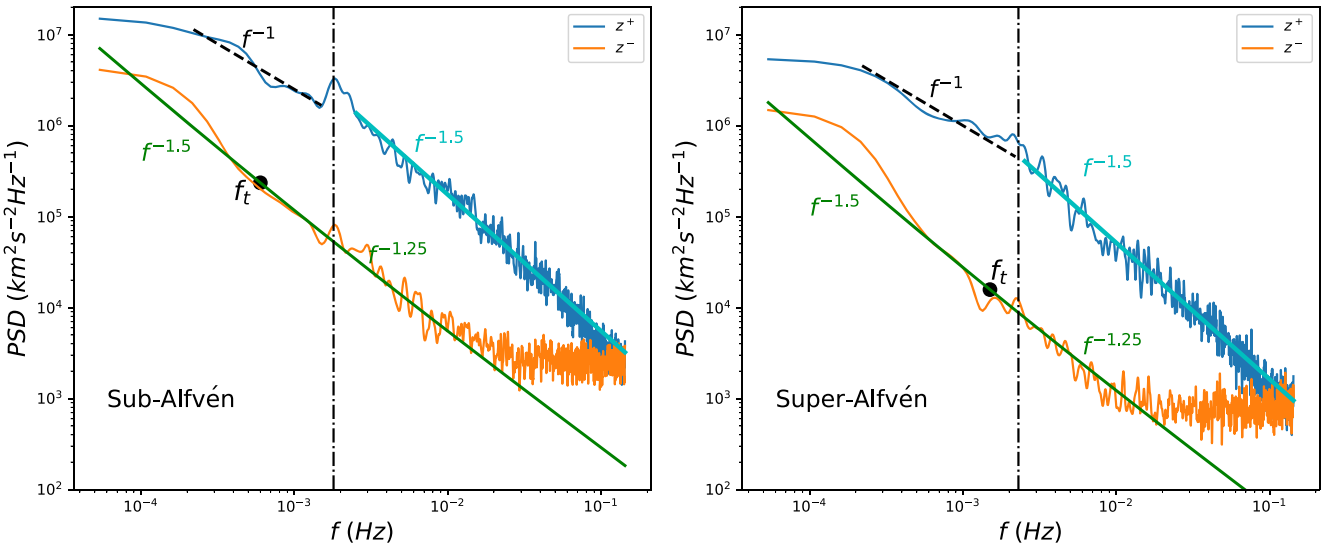

Figure 2. Trace spectra of the Elsässer variables $z^{\pm}$ calculated in 5 hr intervals for the sub-Alfvénic region (left panel) and a neighboring super-Alfvénic region (right panel). The sub-Alfvénic region is delineated by the two vertical dashed lines shown in Figure 1. The 5 hr interval just after the sub-Alfvénic region is selected as representative of the super-Alfvénic region. The solid green and cyan lines are predicted theoretical spectra, the dashed f^{-1} curve is to guide the eye, and f_t identifies the transition frequency (see text for details). The dashed–dotted vertical line separates the f^{-1} and the $f^{-1.5}$ sections of the z^+ spectra.

modestly super-Alfvénic spectra for $z^{\pm}$ are very similar, and the dominance of z^+ is again evident.

Although not the focus of this work, we note that the dominant z^+ spectrum exhibits a low-frequency $f^{-1.0}$ power law, unlike the z^- spectrum. Matteini et al. (2018) offered an interesting explanation for why the dominant slab spectrum should exhibit an $f^{-1.0}$ spectrum and the minority spectrum should not in terms of a saturation of the fluctuation amplitude at large scales imposed by the constraint $\boldsymbol{B} = \text{const}$.

The values of $\Psi \equiv \langle \theta_{B_0 U_0} \rangle$ in the sub- and super-Alfvénic region analyses in Figure 2 are 15° and 18°, respectively. Unfortunately, both the strong alignment of the mean magnetic field and mean velocity and the very limited range of $\theta_{B_0 U_0}$ in both intervals of interest, as shown in Figure 1, make it very difficult to evaluate the ratio of 2D and slab power. To do so requires a wide range of angles $\theta_{B_0 U_0}$ (∼0°–90°), and indeed, Zhao et al. (2020a, 2021a) and Wu et al. (2021) used the criterion $0° < \theta_{B_0 U_0} < 20°$ or $>160°$ to identify parallel intervals. We conclude that because of the parallel sampling in the two sub- and super-Alfvénic intervals, the 2D component is not observed and hence does not contribute significantly to the observed slab component, not allowing us to accurately assess the 2D contribution. Further analysis is needed to clarify this, hopefully with a wider range of sampling angles observed in future sub-Alfvénic flows. From both the values of Ψ and the normalized cross-helicity and residual energy spectrograms, it is clear that the spectra correspond to predominantly forward- and minority backward-propagating Alfvénic fluctuations, since the 2D component is observationally invisible to PSP. While one may argue that the $f^{-3/2}$ z^+ spectrum is consistent with the Iroshnikov–Kraichnan theory, the argument is not credible, since the needed counterpropagating z^- waves are almost entirely absent. The spectral theory of NI MHD (Zank et al. 2020) predicts that the general form of the NI/slab turbulence spectrum is given by

$$G^*(k_z) \equiv E^*(k_z, k_\perp) k_\perp^2 = C^* k_z^{-(2a+3)/3} \left(1 + \left(\frac{k_z}{k_t}\right)^{-(2a-3)/3}\right)^{1/2}, \quad (10)$$

where a describes a possible relationship between slab wavenumbers $k_\perp$ and k_z, i.e., wavenumber anisotropy, such that $k_\perp = k_z^a / k_t^{a-1}$ for $a > 0$. In deriving Equation (10), as with any spectral theory, a crucial step is to identify the triple correlation time τ_3 and then invoke a Kolmogorov phenomenology (Matthaeus & Zhou 1989; Zhou & Matthaeus 1990; Zhou et al. 2004) for the NI/slab model; i.e., the NI/slab dissipation rate ε_* satisfies $\varepsilon_* = \langle z^{*2} \rangle \tau_s = \tau_3 \langle z^{*2} \rangle / \tau_*^2$, where τ_s is the spectral transfer time given by τ_3 / τ_*^2 and τ_* is the dynamical timescale $\tau_*^{-1} \equiv \langle z^{*2} \rangle^{1/2} k_\perp = \tau_3 \langle z^{*2} \rangle^2 k_\perp^2$. Zank et al. (2020) approximated the triple correlation time as the sum $\tau_3^{-1} = \tau_\infty^{-1} + \tau_A^{-1}$, where τ_∞ is the usual nonlinear timescale for the dominant 2D component, $\tau_\infty^{-1} = \langle z^{\infty 2} \rangle^{1/2} / \lambda_\perp^\infty$, and $\lambda_\perp^\infty$ is the corresponding perpendicular correlation length. A somewhat more complicated Alfvénic timescale τ_A is necessary (Zank et al. 2020) because the usual V_A / λ_A, where λ_A is the Alfvénic correlation length, fails to capture two critical properties: (1) the Alfvén advection term does not contribute to nonlinear interactions or spectral transfer for unidirectionally propagating Alfvén waves, and (2) spectral transfer mediated by the Alfvén term is possible only when $\langle z^{*+2} \rangle \neq \langle z^{*-2} \rangle \neq 0$, i.e., for $|\sigma_c^*| \neq 1$, where σ_c^* is the normalized NI/slab cross-helicity. A suitable generalization of the Alfvén timescale that captures the two properties above is given by $\tau_A^{-1} = (V_{A0} / \lambda_A) M_{A0}^{t\,2} (1 - \sigma_c^{*2})^{1/2}$ (Zank et al. 2020),[7] where the subscript zero refers to mean magnetic field values. This then yields Equation (10), which has a "transition wavenumber" k_t or frequency f_t (Figure 2). The physical interpretation of k_t is that it represents the transition from a wavenumber regime controlled primarily by nonlinear interactions to a regime controlled by Alfvénic interactions; specifically, we formally have from the

[7] The parameter $M_{A0}^t = \langle u^2 \rangle^{1/2} / V_{A0}$ is the turbulent Alfvénic Mach number, since $\langle u^2 \rangle$ is the variance of the turbulent velocity fluctuations and represents the scaling parameter used in the NI MHD expansion in the $\beta_p \ll 1$ or $O(1)$ limits (Zank & Matthaeus 1993; Zank et al. 2017, 2020). The presence of the term in the Alfvén timescale is a formal consequence of the NI scaling and has no additional physical significance.

above definitions that $\tau_\infty/\tau_A = (k_z/k_t)^{-(2a-3)/3}$ (Zank et al. 2020).

We can apply Equation (10) to the spectra shown in Figure 2 by choosing $a = 3/4$, i.e., $k_\perp \sim k_z^{3/4}$. For the z^+ spectrum, we assume that $\tau_\infty \ll \tau_A^+$, i.e., nonlinear interactions mediated by quasi-2D fluctuations dominate, and so obtain

$$G^{*+}(k_z) \simeq C^{*+} k_z^{-3/2}. \tag{11}$$

This is reasonable given the absence of sufficient z^- modes with which to interact nonlinearly (Dobrowolny et al. 1980a, 1980b). For the z^- spectrum, we suppose that τ_∞ and τ_A are finite, since the minor z^- component can interact with the more numerous counterpropagating z^+ modes. Thus, there exists a transition wavenumber k_t, after which the z^- spectrum will flatten. Equation (10) becomes

$$G^{*-}(k_z) = C^{*-} k_z^{-3/2}\left(1 + \left(\frac{k_z}{k_t}\right)^{1/2}\right)^{1/2}, \tag{12}$$

showing that at small wavenumbers, the spectrum is $\sim k_z^{-3/2}$, and at large wavenumbers, the asymptotic spectrum is $\sim k_z^{-1.25}$. We use Equations (6)–(9) to express the wavenumber spectra for the 2D component ($C^\infty k_\perp^{-5/3}$) and the slab component (Equations (11) and (12)) in frequency space. The results are illustrated in Figure 2. The left panel for the sub-Alfvénic region shows that the observed $z^\pm$ PSDs are very well fitted by the theory for values of $C^*\pm = 0.13$ and 1.5, respectively, and $k_t = 4.3 \times 10^{-4}$ km^{-1}. The predicted flattening of the theoretical frequency spectrum $f^{-3/2}$ at higher frequencies to $f^{-1.25}$ fits the observed z^- PSD well. The super-Alfvénic interval spectra (right panel) are similarly well fitted with similar parameters $C^*\pm = 0.08$ and 0.012, respectively, and $k_t = 1.0 \times 10^{-4}$ km^{-1}. Since Ψ is essentially parallel in both intervals, the contribution from the 2D spectrum is very small and prevents us from evaluating C^∞. The full anisotropy cannot therefore be determined because we cannot evaluate the power spectrum $P_\perp^\infty(f)$ (Equations (7) and (9)) observationally. The parameter a relating $k_\perp$ and k_z introduces a modest slab anisotropy such that $P_\parallel^*(k_z) > P_\parallel^*(k_\perp)$ at sufficiently small scales. In the context of NI MHD, this implies the ordering $P_\perp^\infty(k_\perp) \gg P_\parallel^*(k_z) > P_\parallel^*(k_\perp)$ with $a = 3/4$ (Zank et al. 2020). As we discuss further below in the physical interpretation, where observations of nonslab turbulence can be made by PSP, a significant quasi-2D component has been observed (Bandyopadhyay & McComas 2021; Zhao et al. 2022).

The fitting parameters apply primarily to the spectral slopes, and although the spectral indices for the $z^\pm$ spectra are similar for both the super- and sub-Alfvénic intervals, there are some obvious differences. For example, the transition frequency f_t shifts to a larger frequency in the super-Alfvénic region, suggesting that nonlinear interactions rather than Alfvénic interactions dominate more of the low-frequency spectrum. In addition, the spectral amplitude in the inertial range for both $z^\pm$ in the sub-Alfvénic region is approximately five times larger than that in the super-Alfvénic region, and this appears to be true of the f^{-1} energy-containing range for the z^+ spectra too.

Shown in Figure 3 are plots of the electron number density PSDs in the sub- and super-Alfvénic regions. Because the partial moment fractions for the PSP/SPAN-Ai data are

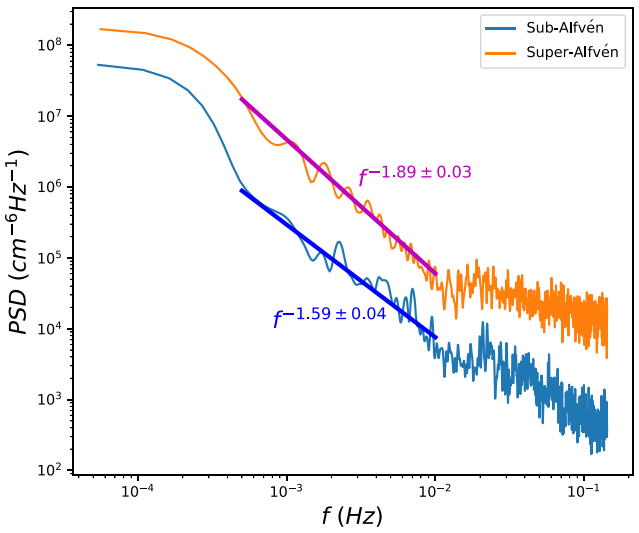

Figure 3. The PSDs for the fluctuating density variance in the sub- and super-Alfvénic regions corresponding to those used for Figure 2. The LFR electron density from FIELDS has been used. The fitted frequency range for both intervals ranges from 5×10^{-4} to 1×10^{-2} Hz.

entangled with the velocity fluctuations, it is difficult to evaluate the extent to which the density fluctuations are or are not passive structures embedded in incompressible turbulence. For this reason, we use the more accurate low-frequency receiver (LFR) electron data set from the Radio Frequency Spectrometer part of the PSP/FIELDS instrument suite (Bale et al. 2016), since it is sufficiently well populated over the range shown in Figure 3. The flattening at higher frequencies beyond some 10^{-2} Hz is likely real despite the LFR data being unreliable at these higher frequencies. (An independent analysis calibrating the LFR measurements to the spacecraft floating voltage and using that as a proxy indicates a high-frequency flattening followed by an eventual steepening of the electron density spectrum. This is not shown here, since it is outside the low-frequency inertial range of turbulence on which we are focused.) The spectra over the interval 4×10^{-4}–10^{-2} Hz are simple power laws with a spectral index of about -1.59 in the sub-Alfvénic flow and about -1.89 in the super-Alfénic flow. The density spectra for both regions do not correspond to the z^+ spectra in the inertial range that have a -1.5 spectral index and are quite unlike the convex z^- spectra (Figure 2), thus ruling out the possibility that the density spectra are due to the parametric decay instability (Goldstein 1978; Telloni et al. 2009; Bruno et al. 2014). Density spectra can be determined from the NI MHD theory. Within the NI MHD theory, density fluctuations are entropic modes, i.e., zero-frequency fluctuations, that are advected by the dominant quasi-2D turbulent velocity fluctuations and therefore behave as a passive scalar (Zank et al. 2017). The relevant timescale is the quasi-2D nonlinear timescale, and the underlying spectrum responsible for advection is that associated with the 2D velocity fluctuations. The NI MHD theory explicitly shows that the 2D Elsässer variable spectrum satisfies $E_{2D} \sim k_\perp^{-5/3}$. Under some circumstances (Zank et al. 2017), this serves as a proxy for the spectrum of 2D velocity fluctuations, but more generally, the dominant quasi-2D velocity spectrum $E_{2D,v}$ will have the form $E_{2D,v} \sim k_\perp^{-q}$. This yields a density spectrum of the form $E_\rho(k_\perp) = C_\rho k_\perp^{-q}$, where $q = 5/3$ only if, e.g., kinetic

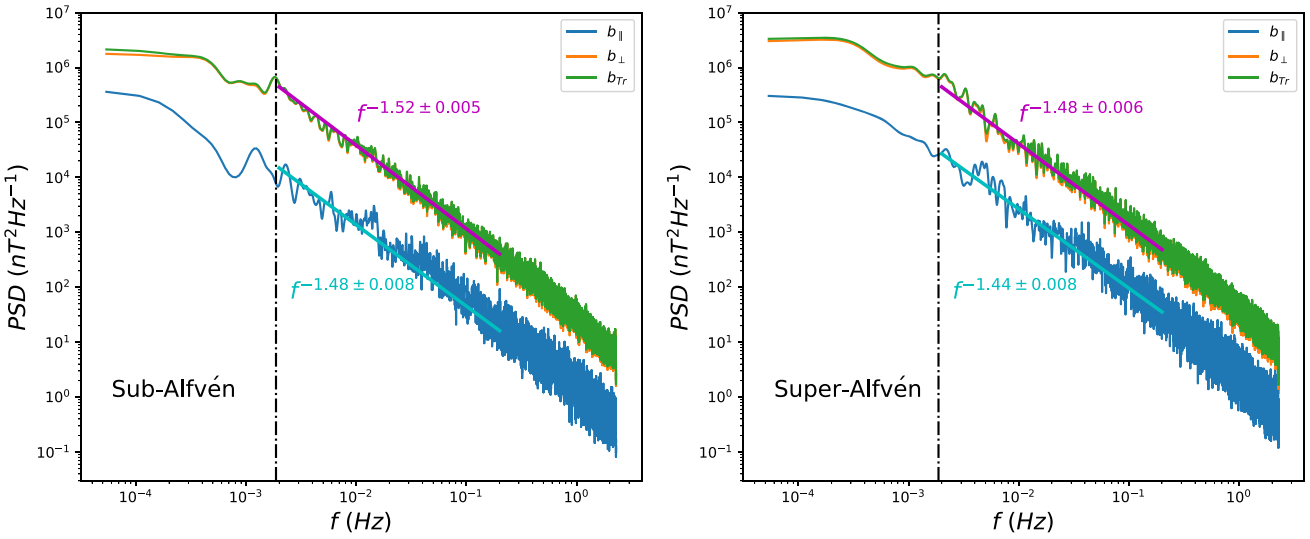

Figure 4. The PSDs for magnetic fluctuations in the parallel (blue) and transverse (orange) directions for the sub-Alfvénic (left panel) and super-Alfvénic (right) regions. The total trace spectrum (green) effectively overlays the transverse fluctuations. Pink and blue lines are fitted to the data over the frequency range 2×10^{-3}–0.2 Hz to estimate the spectral indices of the incompressible and compressible magnetic field PSDs.

energy dominates or the quasi-2D residual energy is zero. By extending the analysis of Section 2, one can show that the frequency spectrum for the density PSD $P_\rho(f)$ is related to the density wavenumber PSD $P_\rho(k_\perp)$ according to

$$P_\rho(f) = C_\rho \int_{|k_x|}^{\infty} \frac{k_\perp^{-q}}{\sqrt{k_\perp^2 - k_x^2}} dk_\perp = \frac{\sqrt{\pi} C_\rho k_x^{-q} \Gamma\left(\frac{q}{2}\right)}{2\Gamma\left(\frac{q+1}{2}\right)}, \quad k_x = \frac{2\pi f}{U_0 \sin\Psi}, \tag{13}$$

where C_ρ is the amplitude of the density spectrum. The frequency spectrum therefore has the form f^{-q}. That the density spectrum is noticeably distinct from both the observed $z^\pm$ spectra suggests that its origin is unrelated to the slab spectra, whether via the parametric decay instability or passive advection of density fluctuations by slab turbulence. That leaves the possibility that the density fluctuations are either zero-frequency NI MHD entropic modes advected by quasi-2D incompressible turbulence (Zank et al. 2017) or compressible wave modes, which have been identified in PSP data in the presence of dominant incompressible turbulence (Zhao et al. 2021b).

The compressibility of the fluctuations is presented in Figure 4, illustrating that the transverse or incompressible magnetic fluctuations, shown by the orange curve, are clearly dominant compared to the compressible magnetic field-aligned fluctuations (blue curve). This is true of both sub- and super-Alfvénic regions and consistent with observations discussed previously by Zhao et al. (2021b). This assures us that the turbulence observed by PSP is largely incompressible, including in the sub-Alfvénic solar wind. The spectral slopes are found to be about -1.52 for incompressible magnetic fluctuations and about -1.48 for the corresponding compressible component in the sub-Alfvénic wind and, respectively, -1.48 and -1.44 in the super-Alfvénic interval over the frequency range 2×10^{-3}–0.2 Hz. It is evident that the spectral indices of the observed density PSDs are quite different from those of the compressible spectra shown in Figure 4. Whereas the compressible fluctuations shown in Figure 4 can be associated with fast (and possibly slow) magnetosonic modes (Zhao et al. 2021b), the very different characteristics of the density PSDs suggest that these fluctuations are not associated with waves but instead are likely to be entropy fluctuations with zero frequency. This result demonstrates ex post facto the rationale for using Taylor's hypothesis for density fluctuations in the form of Equation (13), i.e., for advected density fluctuations. Within NI MHD, density fluctuations are advected by the dominant quasi-2D turbulence in the $O(1)$ and $\ll 1$ plasma beta regimes (Hunana & Zank 2010; Zank et al. 2017), thereby providing insight into the dominant quasi-2D velocity turbulence that PSP is unable to observe in the highly field-aligned intervals. In particular, the density spectrum in the sub-Alfvénic region suggests a quasi-2D velocity spectrum very slightly flatter than $-5/3$ and rather steeper than $-5/3$ in the super-Alfvénic interval.

Evidence for the presence of quasi-2D fluctuations has been presented elsewhere. Zhao et al. (2020a, 2020b, 2021b) identified small-scale flux ropes observed in previous PSP encounters. Bandyopadhyay & McComas (2021) and Zhao et al. (2022) found that turbulence in the inner heliosphere is highly anisotropic with significant contributions from a quasi-2D component, in many cases dominating the slab contribution despite the challenges for PSP observing quasi-2D fluctuations when the magnetic field and plasma flow become increasingly highly aligned with decreasing distance above the solar surface. Accordingly, we can interpret the spectra illustrated in Figure 2 as due to the possibly minority slab component of quasi-2D +slab turbulence. This then yields the following physical interpretation of the observed $z^\pm$ turbulent fluctuations in the sub-Alfvénic and modestly super-Alfvénic regions of the solar wind. The z^+ (outward) fluctuations dominate, with the spectral amplitude of inward-propagating slab modes nearly an order of magnitude smaller, meaning the slab component is comprised

almost entirely of unidirectionally propagating Alfvén waves. Given the much smaller intensity of inward-propagating modes, the z^+ are obliged to interact nonlinearly almost exclusively with quasi-2D modes to produce the observed power-law spectrum. The nonlinear interaction is governed by the nonlinear timescale τ_∞ with virtually no interaction on the Alfvén timescale τ_A with the counterpropagating minority z^- component. The spectral slope of $-3/2$ for z^+ (and the low-frequency part of the z^- spectrum) indicates modest slab wavenumber anisotropy with $k_z \sim k_\perp^{4/3}$ in the inertial range. By contrast, the low-frequency z^- component is dominated by nonlinear rather than Alfvénic interactions, unlike the high frequencies that are governed primarily by interactions with counterpropagating Alfvén modes on the timescale τ_A^-. This is manifest in the concavity of the z^- spectrum due to the presence of a transition wavenumber or frequency at which $\tau_\infty = \tau_A$. Nonetheless, to explain the slab observations presented here in the context of NI MHD, the 2D component power anisotropy should dominate the power in the slab component.

4. Conclusions

1. The spectrograms for the normalized magnetic helicity σ_m, cross-helicity σ_c, and residual energy σ_r show that PSP observed primarily outwardly propagating Alfvénic fluctuations during the first of the sub-Alfvénic intervals observed. This likely reflects the highly magnetic field-aligned flow of the interval that renders quasi-2D fluctuations effectively invisible to observations. Nonetheless, some evidence of magnetic structures is present near the interval boundaries, as well as a large vortex-like structure embedded in the interval.
2. We extended Taylor's hypothesis, allowing us to relate frequency and wavenumber spectra in our analysis of turbulence in sub-Alfvénic and the modestly super-Alfvénic flows, based on a decomposition of the turbulence into 2D and forward- and backward-propagating slab components.
3. The PSDs for the $z^\pm$ (Elsässer) fluctuations were plotted for sub- and super-Alfvénic intervals, showing that the forward z^+ component dominates, having a spectral amplitude much greater than that of the z^- PSD, and a frequency (wavenumber) spectrum of the form $f^{-3/2}$ ($k_\parallel^{-3/2}$) throughout the inertial range. By contrast, the z^- PSD exhibits a convex spectrum, $f^{-3/2}$ ($k_\parallel^{-3/2}$), at low frequencies that flattens around a transition frequency (wavenumber) f_t (k_t) to $f^{-1.25}$ ($k_\parallel^{-1.25}$) at higher frequencies. Because PSP makes measurements in a highly aligned flow, the observations correspond largely to slab fluctuations.
4. To interpret the observations, we apply the NI MHD 2D +slab spectral theory (Zank et al. 2020) to the $z^\pm$ spectra, finding that the theoretically predicted slab spectra are in excellent agreement with the observed spectra if there exists a modest slab wavenumber anisotropy $k_\perp \sim k_\parallel^{3/4}$. The z^+ wavenumber spectrum is predicted to be $k_\parallel^{-3/2}$ because it interacts primarily with quasi-2D fluctuations on a timescale τ_∞ rather than the significantly smaller z^- component. By contrast, the minority z^- fluctuations can interact with both quasi-2D and counterpropagating slab modes, so that both the nonlinear τ_∞ and Alfvén τ_A timescales determine the form of the spectrum. Theoretically, this combination of timescales predicts a convex spectrum with the inflection or transition point determined by the balance of the timescales, $\tau_\infty = \tau_A$, and the spectrum is predicted to flatten from an $f^{-3/2}$ ($k_\parallel^{-3/2}$) low-frequency or nonlinear-dominated regime to an $f^{-1.25}$ ($k_\parallel^{-1.25}$) higher-frequency or Alfvénic-dominated regime. Plots of the transverse and compressible magnetic field fluctuations show that turbulence in the sub- and modestly super-Alfvénic flows are dominated by incompressible fluctuations.
5. The PSDs for the density fluctuations were plotted for both intervals of interest, exhibiting simple power laws with spectral indices of -1.59 and -1.89 for the sub- and super-Alfvénic cases, respectively. The spectra do not resemble the dominant z^+ PSD and are distinctly different from the convex structured z^- spectrum, suggesting that the density fluctuations are not due to the parametric decay instability. The compressible magnetic field fluctuation spectrum follows the incompressible magnetic field spectrum closely and is distinctly different from the density spectrum, suggesting that the density fluctuations are not primarily compressible magnetosonic wave modes. Instead, they appear to be zero-frequency entropic modes advected by the background turbulent velocity field. This interpretation is consistent with the expectations of NI MHD in which entropic density fluctuations are advected by the dominant quasi-2D velocity fluctuations, indicating that the density spectra offer insight into quasi-2D turbulence.
6. We find that the spectra in the neighboring modestly super-Alfvénic regions closely resemble those in the sub-Alfvénic interval, and indeed, the three parameters ($C^{*\pm}$ and a) for the two sets of spectra are very similar, indicating that the same basic turbulence physics holds in both regions. Nonetheless, there are some differences in the details, such as the transition frequency shifting to a larger frequency in the super-Alfvénic region, and the fluctuating power for both z^+ and z^- in the sub-Alfvénic region is approximately five times larger than that in the super-Alfvénic region. The larger k_t for the super-Alfvénic flow indicates that nonlinear interactions rather than Alfvénic interactions dominate for a larger part of the low-frequency spectrum.
7. The physical interpretation of the Elsässer forward and backward slab and density spectra reflects a manifestation of dominant quasi-2D turbulent fluctuations in the solar wind. The same parameters explain both the observed forward and backward Elsässer spectra. Since the fitting of the results is predicated on a quasi-2D nonlinear timescale and a quasi-2D spectrum of the Kolmogorov form, the results presented here suggest the presence of a dominant 2D component that, because of the field-aligned sampling in both intervals during this encounter, cannot be observed by PSP but nevertheless controls the evolution of slab and density turbulence in the sub-Alfvénic solar wind.

G.P.Z., L.L.Z., and L.A. acknowledge the partial support of NASA Parker Solar Probe contract SV4-84017, NSF EPSCoR RII-Track-1 cooperative agreement OIA-1655280, a NASA IMAP subaward under NASA contract 80GSFC19C0027, and

NASA award 80NSSC20K1783. D.T. was partially supported by the Italian Space Agency (ASI) under contract 2018-30-HH.0. The Parker Solar Probe was designed and built and is now operated by the Johns Hopkins Applied Physics Laboratory as part of NASA's Living with a Star (LWS) program (contract NNN06AA01C). Support from the LWS management and technical team has played a critical role in the success of the Parker Solar Probe mission.

ORCID iDs

G. P. Zank https://orcid.org/0000-0002-4642-6192
L.-L. Zhao https://orcid.org/0000-0002-4299-0490
L. Adhikari https://orcid.org/0000-0003-1549-5256
D. Telloni https://orcid.org/0000-0002-6710-8142
J. C. Kasper https://orcid.org/0000-0002-7077-930X
M. Stevens https://orcid.org/0000-0002-7728-0085
A. Rahmati https://orcid.org/0000-0003-0519-6498
S. D. Bale https://orcid.org/0000-0002-1989-3596

References

Bale, S. D., Goetz, K., Harvey, P. R., et al. 2016, SSRv, 204, 49
Bandyopadhyay, R., & McComas, D. J. 2021, ApJ, 923, 193
Bieber, J. W., Matthaeus, W. H., Smith, C. W., et al. 1994, ApJ, 420, 294
Bieber, J. W., Wanner, W., & Matthaeus, W. H. 1996, JGR, 101, 2511
Bourouaine, S., & Perez, J. C. 2020, ApJL, 893, L32
Bruno, R., Telloni, D., Primavera, L., et al. 2014, ApJ, 786, 53
Burlaga, L., Sittler, E., Mariani, F., & Schwenn, R. 1981, JGR, 86, 6673
Chandran, B. D. G., & Perez, J. C. 2019, JPlPh, 85, 905850409
Cranmer, S. R., & van Ballegooijen, A. A. 2012, ApJ, 754, 92
Dobrowolny, M., Mangeney, A., & Veltri, P. 1980a, PhRvL, 45, 144
Dobrowolny, M., Mangeney, A., & Veltri, P. 1980b, A&A, 83, 26
Goldreich, P., & Sridhar, S. 1995, ApJ, 438, 763
Goldstein, M. L. 1978, ApJ, 219, 700
Hunana, P., & Zank, G. P. 2010, ApJ, 718, 148
Kasper, J. C., Abiad, R., Austin, G., et al. 2016, SSRv, 204, 131
Kasper, J. C., Klein, K. G,, Lichko, E., et al. 2021, PhRvL, 127, 255101
Klein, K. G., Perez, J. C., Verscharen, D., Mallet, A., & Chandran, B. D. G. 2015, ApJL, 801, L18
Matteini, L., Stansby, D., Horbury, T. S., & Chen, C. H. K. 2018, ApJL, 869, L32
Matthaeus, W. H., Goldstein, M. L., & Roberts, D. A. 1990, JGR, 95, 20673
Matthaeus, W. H., Goldstein, M. L., & Smith, C. 1982, PhRvL, 48, 1256
Matthaeus, W. H., & Smith, C. 1981, PhRvA, 24, 2135
Matthaeus, W. H., Zank, G. P., Oughton, S., Mullan, D. J., & Dmitruk, P. 1999, ApJL, 523, L93
Matthaeus, W. H., & Zhou, Y. 1989, PhFlB, 1, 1929
Moldwin, M. B., Phillips, J. L., Gosling, J. T., et al. 1995, JGR, 100, 19903
Saur, J., & Bieber, J. W. 1999, JGR, 104, 9975
Shebalin, J. V., Matthaeus, W. H., & Montgomery, D. 1983, JPlPh, 29, 525
Shoda, M., Yokoyama, T., & Suzuki, T. K. 2018, ApJ, 853, 190
Telloni, D., Bruno, R., Carbone, V., Antonucci, E., & D'Amicis, R. 2009, ApJ, 706, 238
Telloni, D., Bruno, R., D'Amicis, R., Pietropaolo, E., & Carbone, V. 2012, ApJ, 751, 19
Telloni, D., Carbone, F., Bruno, R., et al. 2019, ApJ, 887, 160
Telloni, D., Perri, S., Bruno, R., Carbone, V., & Amicis, R. D. 2013, ApJ, 776, 3
Verdini, A., Velli, M., & Buchlin, E. 2009, ApJL, 700, L39
Wang, X., Tu, C., He, J., et al. 2015, ApJL, 810, L21
Wu, H., Tu, C., Wang, X., & Yang, L. 2021, ApJ, 911, 73
Zank, G. P., Adhikari, L., Hunana, P., et al. 2017, ApJ, 835, 147
Zank, G. P., Adhikari, L., Zhao, L. L., et al. 2018, ApJ, 869, 23
Zank, G. P., & Matthaeus, W. H. 1992, JGR, 97, 17189
Zank, G. P., & Matthaeus, W. H. 1993, Phys. Fluids, 5, 257
Zank, G. P., Nakanotani, M., Zhao, L. L., Adhikari, L., & Telloni, D. 2020, ApJ, 900, 115
Zank, G. P., Zhao, L. L., Adhikari, L., et al. 2021, PhPl, 28, 080501
Zhao, L. L., Zank, G. P., Adhikari, L., & Nakanotani, M. 2022, ApJL, 924, L5
Zhao, L. L., Zank, G. P., Adhikari, L., et al. 2020a, ApJ, 898, 113
Zhao, L. L., Zank, G. P., Adhikari, L., et al. 2020b, ApJS, 246, 26
Zhao, L. L., Zank, G. P., He, J. S., et al. 2021a, ApJ, 922, 188
Zhao, L. L., Zank, G. P., Hu, Q., et al. 2019, ApJ, 886, 144
Zhao, L. L., Zank, G. P., Hu, Q., et al. 2021b, A&A, 650, A12
Zhou, Y., & Matthaeus, W. H. 1990, JGR, 95, 14881
Zhou, Y., Matthaeus, W. H., & Dmitruk, P. 2004, RvMP, 76, 1015